



**Anomalous Isoelectronic Chalcogen Rejection in 2D  
Anisotropic vdW TiS<sub>3</sub>(1-x)Se<sub>3x</sub> Trichalcogenides**

Journal:	<i>Nanoscale</i>
Manuscript ID	NR-ART-05-2018-004274.R2
Article Type:	Paper
Date Submitted by the Author:	31-Jul-2018
Complete List of Authors:	Agarwal, Ashutosh; Arizona State University Qin, Ying; Arizona State University Chen, Bin; Arizona State University, Materials Science and Engineering Blei, Mark; Arizona State University, School for Engineering of Matter, Transport and Energy Wu, Kedi; Arizona State University, Liu, Lei; Arizona State University Shen, Yuxia; Arizona State University, Wright, David; Arizona State University, Materials Science and Engineering Green, Matthew; Arizona State University, Chemical Engineering Zhuang, Houlong; Arizona State University, Tongay, Sefaattin; University of California, Berkeley, Materials Science and Engineering

## Anomalous Isoelectronic Chalcogen Rejection in 2D Anisotropic vdW $\text{TiS}_{3(1-x)}\text{Se}_{3x}$ Trichalcogenides

Ashutosh Agarwal<sup>1</sup>, Ying Qin<sup>1</sup>, Bin Chen<sup>1</sup>, Mark Blei<sup>1</sup>, Kedi Wu<sup>1</sup>, Lei Liu<sup>1</sup>, Yuxia Shen<sup>1</sup>, David Wright<sup>2</sup>, Matthew D. Green<sup>1</sup>, Houlong Zhuang<sup>1</sup>, and Sefaattin Tongay<sup>1,\*</sup>

<sup>1</sup> School for Engineering of Matter, Transport and Energy, Arizona State University, Tempe, Arizona 85287, USA

<sup>2</sup> LeRoy Eyring Center for Solid State Science, Arizona State University, Tempe, Arizona 85287, USA

\* corresponding authors: sefaattin.tongay@asu.edu

### Abstract

Alloying in semiconductors has enabled many civilian technologies in electronics, optoelectronics, photonics, and others. While the alloying phenomenon is well established in traditional bulk semiconductors owing to a vast array of available ternary phase diagrams, alloying in 2D materials still remains at its seminal stages. This is especially true for transition metal trichalcogenides (TMTCs) such as  $\text{TiS}_3$  which has been recently predicted to be a direct gap, high carrier mobility, pseudo-1D semiconductor. In this work, we report on an unusual alloying rejection behavior in  $\text{TiS}_{3(1-x)}\text{Se}_{3x}$  vdW crystals. TEM, SEM, EDS, and angle-resolved Raman measurements show that only a miniscule amount (8%) of selenium can be successfully alloyed into a  $\text{TiS}_3$  host matrix despite vastly different precursor amounts as well as growth temperatures. This unusual behavior contrasts with other vdW systems such as  $\text{TiS}_{2(1-x)}\text{Se}_{2x}$ ,  $\text{MoS}_{2(1-x)}\text{Se}_{2x}$ ,  $\text{Mo}_{1-x}\text{W}_x\text{S}_2$ ,  $\text{WS}_{2(1-x)}\text{Se}_{2x}$ , where continuous alloying can be attained. Angle-resolved Raman and kelvin probe force microscopy measurements offer insights into how selenium alloying influences in-plane structural anisotropy as well as electron affinity values of exfoliated sheets. Our cluster expansion theory calculations show that only the alloys with a small amount of Se can be attained due to energetic instability above / below a certain selenium concentration threshold in the ternary phase diagrams. The overall findings highlight potential challenges in achieving stable Ti based TMTCs alloys.

### Introduction

Alloying in solid material systems allows for reproducible and scalable ways to engineer the fundamental properties of materials for a variety of targeted applications. While our knowledge on the phase diagrams and alloying of traditional bulk material systems are relatively well-established, it is still at its seminal stages for vdW crystals and two-dimensional (2D) materials<sup>1</sup>. To date, a number of transition metal dichalcogenides (TMDCs) ternary alloys such as  $\text{MoS}_{2(1-x)}\text{Se}_{2x}$ ,  $\text{Mo}_{1-x}\text{W}_x\text{S}_2$ ,  $\text{WS}_{2(1-x)}\text{Se}_{2x}$ , and  $\text{TiS}_{2(1-x)}\text{Se}_{2x}$ <sup>[13]</sup> have been demonstrated in the bulk or monolayer form through chemical vapor transport (CVT) and chemical vapor deposition (CVD) techniques, respectively<sup>2-7</sup>. These 2D ternary alloys exhibited full continuous alloying across the entire composition range with band gap coverage in the visible spectrum.

Compared to conventional 2D isotropic material systems, such as  $\text{MoS}_2$ , boron nitride (h-BN), and graphene, transition metal trichalcogenides (TMTCs) show striking structural / crystallographic differences<sup>8</sup>. Metal ions within individual 2D layers exhibit strong Peierls-like structural distortion, and consequently they form pseudo-1D chains extending along one lattice direction (*aka* chain direction). Structural anisotropy in the basal plane (Figure 1a) manifests itself in directionally-dependent physical properties including high mobility carriers<sup>9,10</sup>, thermally conducting channels<sup>11,12</sup>, as well as anisotropic excitons<sup>13,14</sup>. In particular,  $\text{TiS}_3$  has been predicted to be a 1.1 eV direct gap semiconductor (experimental 1.0 eV<sup>15</sup>) with carrier mobility values reaching 11,000  $\text{V}\cdot\text{s}/\text{cm}^2$  which is a potentially exciting direction towards nanoelectronics and optoelectronic applications<sup>9,16-18</sup>. Moreover, experimental studies have shown directionally dependent vibrational response, thermal properties, and electronic performance<sup>8</sup>.

However, 2D alloys of  $\text{TiS}_3$  material systems have not been reported to date, and it still remains unknown if isoelectronic elements can be successfully alloyed or crystallized in pseudo-1D geometry without sacrificing the much desired structural anisotropy. The ability to create ternary alloys of TMTCs enables one to access a broad range of electronic band gap values which falls in the infrared (IR) for Ti-based TMTCs, and thus highly relevant to communication technologies, national security, bolometer, and IR detector technologies.

Here, we report on anomalous isoelectronic chalcogen rejection in TMTCs  $\text{TiS}_{3(1-x)}\text{Se}_{3x}$  ternary alloy systems. Our TEM, SEM, XRD, and EDS results show that surprisingly only a set amount of isoelectronic selenium ( $\sim 8\%$ ) can be incorporated into  $\text{TiS}_3$  sheets despite widely different growth conditions. Angle-resolved Raman (ARR) spectroscopy and selective area diffraction (SAED) measurements show that selenium atoms are successfully incorporated into the host matrix and the anisotropic nature of the  $\text{TiS}_3$  sheets is well-preserved. Our cluster expansion theory calculations further show rather unusual alloying energetics which produces a narrow selenium solubility range. Our experimental and cluster expansion theory results agree well and provide insights into alloying in TMTCs. The overall results not only offer insights into  $\text{TiS}_3$  based alloy systems but our findings can also be used as a guideline for other TMTCs systems.

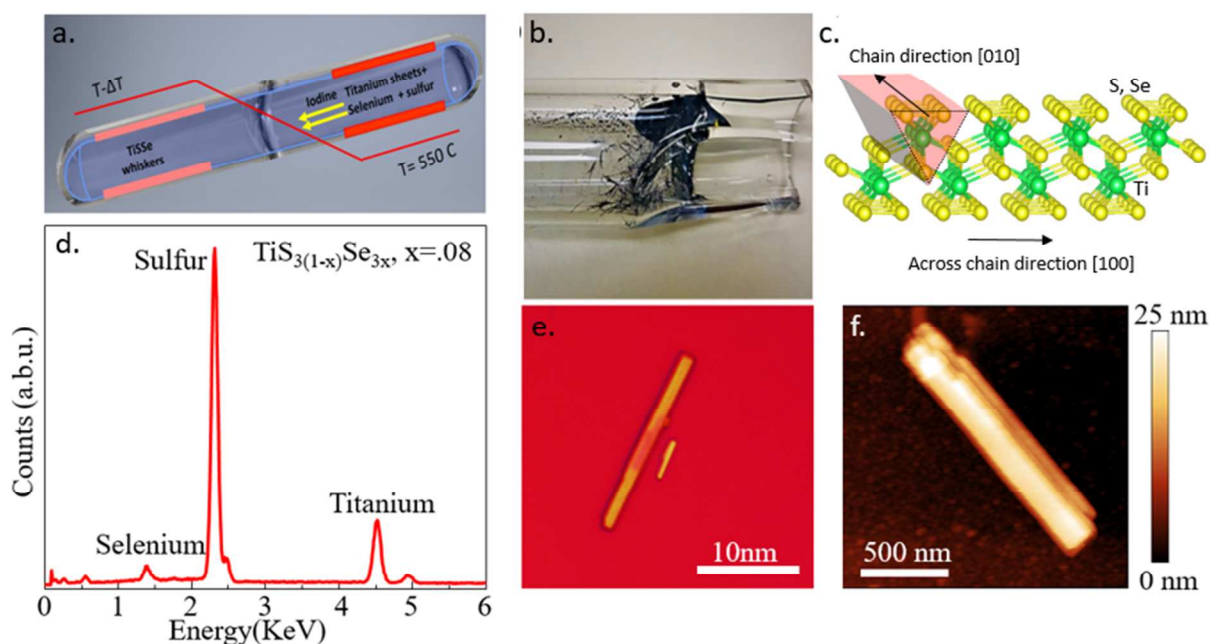


**Figure 1** **a.** Schematic of two zone CVT furnace for the growth of  $\text{TiS}_{2.76}\text{Se}_{0.24}$  **b.** Optical image of  $\text{TiS}_{2.76}\text{Se}_{0.24}$  grown on the inner walls of quartz ampoule **c.** Schematic description of the crystal structure of  $\text{TiS}_{2.76}\text{Se}_{0.24}$  **d.** EDS analysis of  $\text{TiS}_{2.76}\text{Se}_{0.24}$  showing its chemical composition **e.** Optical and **f.** AFM image of  $\text{TiS}_{2.76}\text{Se}_{0.24}$  flake exfoliated onto  $\text{SiO}_2$  substrates with thickness of  $\sim 15\text{nm}$ .

**Crystal growth.** 2D  $\text{TiS}_3$  is a direct band gap of 1.06 eV (theory) and monolayer  $\text{TiSe}_3$  is an indirect band gap of 0.57 eV. Theoretically,  $\text{TiS}_3$  and  $\text{TiSe}_3$  have been predicted to crystallize in a monoclinic crystal structure ( $C_{2h}^2$  ( $P2_1/m$ ) space group). While this has been confirmed on  $\text{TiS}_3$  many decades ago,  $\text{TiSe}_3$  crystals and monolayers are still waiting to be experimentally realized. With the predicted isostructural characteristics of both  $\text{TiS}_3$  and  $\text{TiSe}_3$ , successfully alloying in  $\text{TiS}_{3(1-x)}\text{Se}_{3x}$  across  $x=0$  ( $\text{TiS}_3$ ) to  $x=1$  ( $\text{TiSe}_3$ ) would open a new-class of 2D infrared (IR) semiconductors for defense and IR detector applications.

As shown in Figure 1a, the chemical vapor transport (CVT) method was used to synthesize  $\text{TiS}_{3(1-x)}\text{Se}_{3x}$  ternary alloys (see methods). A quartz ampoule 1.5 cm in diameter and 21 cm in length containing carbonic acid was sonicated for 30 min and then rinsed with IPA and DI water to ensure no dust particles were present inside the ampoule. Next the ampoule was heated to 110 °C for 24 hours to evaporate any residue. Sulfur and selenium pellets, and titanium sheets (all rated 99.9995% purity) were loaded into the ampoule at different ratios. We note that in a typical vdW crystal growth, changes made in the precursor molar ratio or growth temperature allow for composition engineering as demonstrated by our team as well as others<sup>5,7</sup>. The ampoule was sealed with iodine as the transport agent at  $10^{-5}$  Torr, and the loaded ampoule was placed in a two-zone furnace. The hot zone of the ampoule containing all the precursors was kept at  $550 \pm 1$  °C with a temperature gradient of  $4.5 \pm 0.1$  °C/cm (cold / crystallization zone at 450 °C) for seven (7) days.

Typical growth resulted in highly crystalline whisker like crystal formation at the cold end of the ampoule as shown in **Figure 1b-c**. The elemental composition was confirmed through EDS / SEM measurements (**Figure 1d**). Synthesized crystals were lamellar (layered) in nature which can easily be isolated to few-layers by the simple mechanical exfoliation technique (**Figure 1e-f**). As demonstrated by our atomic force microscopy measurements (**Figure 1f**), the exfoliated  $\text{TiS}_{3(1-x)}\text{Se}_{3x}$  sheets exhibited atomically sharp and smooth surfaces. The synthesized crystals as well as exfoliated sheets had a high geometrical aspect ratio with the chain axis oriented in the long direction of the nanoribbons, and these will be discussed later in the article in angle-resolved Raman measurements.

Interestingly, however, synthesized  $\text{TiS}_{3(1-x)}\text{Se}_{3x}$  crystals all crystallized with the alloying composition of  $x=0.08$  despite vastly different growth conditions undertaken during the crystal synthesis. For example, a wide range of growth parameters were systematically tested numerous times by varying hot and cold zone temperatures from 450 °C to 650 °C as well as changing the amount of selenium from 20–80%. We note that at temperatures greater than 590 °C trichalcogenides materials become energetically unstable and immediately transform into  $\text{TiS}_2$  and  $\text{TiSe}_2$  dichalcogenide forms. Growth at different temperatures ( $T_{c,h} < 590$  °C) all produced crystalline  $\text{TiS}_{3(1-x)}\text{Se}_{3x}$  alloy with  $x=0.08$  (**Figure 1d**). This finding suggests that more than 8% selenium is immiscible in a  $\text{TiS}_3$  matrix. This is in stark contrast to many other 2D material systems such as  $\text{TiS}_{2(1-x)}\text{Se}_{2x}$ ,  $\text{MoS}_{2(1-x)}\text{Se}_{2x}$ ,  $\text{Mo}_{1-x}\text{W}_x\text{S}_2$ , and  $\text{WS}_{2(1-x)}\text{Se}_{2x}$ , wherein continuous compositional variation was easily attained during CVT or CVD processes either by fine tuning the growth temperature to change reaction rates of an individual precursor or by adjusting the precursor amount to push one of the precursors to the mass-transport limited regime.

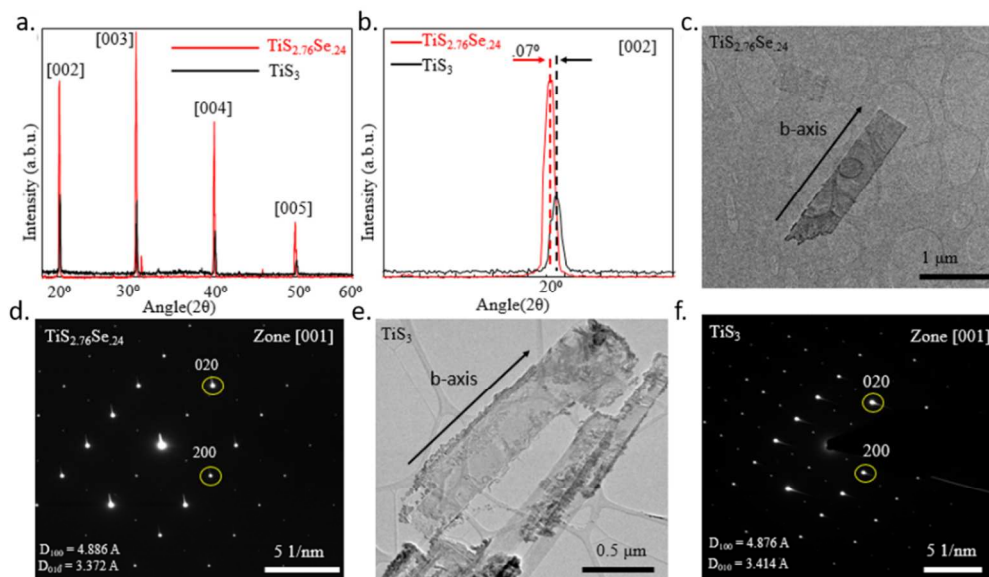


**Figure 2** a. XRD pattern of  $\text{TiS}_{2.76}\text{Se}_{.24}$  (red) and  $\text{TiS}_3$  (black) b. XRD [002] peak of  $\text{TiS}_{2.76}\text{Se}_{.24}$  (red) and  $\text{TiS}_3$  (black). c. TEM image of  $\text{TiS}_{2.76}\text{Se}_{.24}$  d. Electron diffraction pattern of the  $\text{TiS}_{2.76}\text{Se}_{.24}$  e. TEM image of the  $\text{TiS}_3$  sample f. Electron diffraction pattern of the  $\text{TiS}_3$

**Crystal structure and Vibrational properties.** Overall, the  $\text{TiS}_{3(1-x)}\text{Se}_{3x}$  alloy is highly crystalline and has the same monoclinic crystal structure as  $\text{TiS}_3$  as evidenced by similar XRD patterns in **Figure 2a**. The comparison between XRD datasets from  $\text{TiS}_3$  and  $\text{TiS}_{3(1-x)}\text{Se}_{3x}$  show [00/] XRD peaks all shift to smaller  $2\theta$  values when selenium atoms are incorporated into  $\text{TiS}_3$  (**Figure 2b**). This is consistent with increased interlayer spacing due to the much larger Bohr radius of selenium atoms, which is anticipated to increase the interlayer separation. Both  $\text{TiS}_3$  and  $\text{TiS}_{3(1-x)}\text{Se}_{3x}$  still display similar full width at half maxima (FWHM $\sim$ 0.017 $\square$ ) for XRD peaks, and thus similar structural quality is obtained and the crystallite sizes are on the same order of magnitude. Larger amount of XRD intensity in  $\text{TiS}_{3(1-x)}\text{Se}_{3x}$  is mostly related to amount of material measured as well as different XRD scattering cross-sections. After selenium is alloyed into  $\text{TiS}_3$ , Raman peaks shown in **Figure 3** shift to lower frequencies (red-shift) due to heavier effective mass values.

To further assess the crystallinity, we have performed SAED measurements on  $\text{TiS}_3$  and  $\text{TiS}_{3(1-x)}\text{Se}_{3x}$  nanoflakes transferred onto TEM grids using the polymer assisted transfer technique (**Figure 2d,f**). Here, we note that under electron irradiation TMTCs underwent quick structural decomposition, which prevented the collection of reliable atomic resolution images. Nevertheless, SAED diffraction patterns in **Figure 2e** and **Figure 2g** clearly show both  $\text{TiS}_3$  and  $\text{TiS}_{3(1-x)}\text{Se}_{3x}$  crystallize in the monoclinic crystal structure and exhibit well-defined diffraction spots further highlighting the crystallinity of synthesized sheets. Overall,  $\text{TiS}_{3(1-x)}\text{Se}_{3x}$  sheets exhibited larger lattice constant across the chain direction (which is labelled as [100] in **Figure 1c**) compared to the host  $\text{TiS}_3$  semiconductor (**Figure 2f**). While the larger lattice constant across the chain direction [100] points towards an increased pseudo-1D chain separation distance possibly due to larger selenium atoms, the reduced [010] unit cell size remains less clear but potentially related to complex metal-chalcogen, chalcogen-chalcogen, and metal-metal bonding changes.

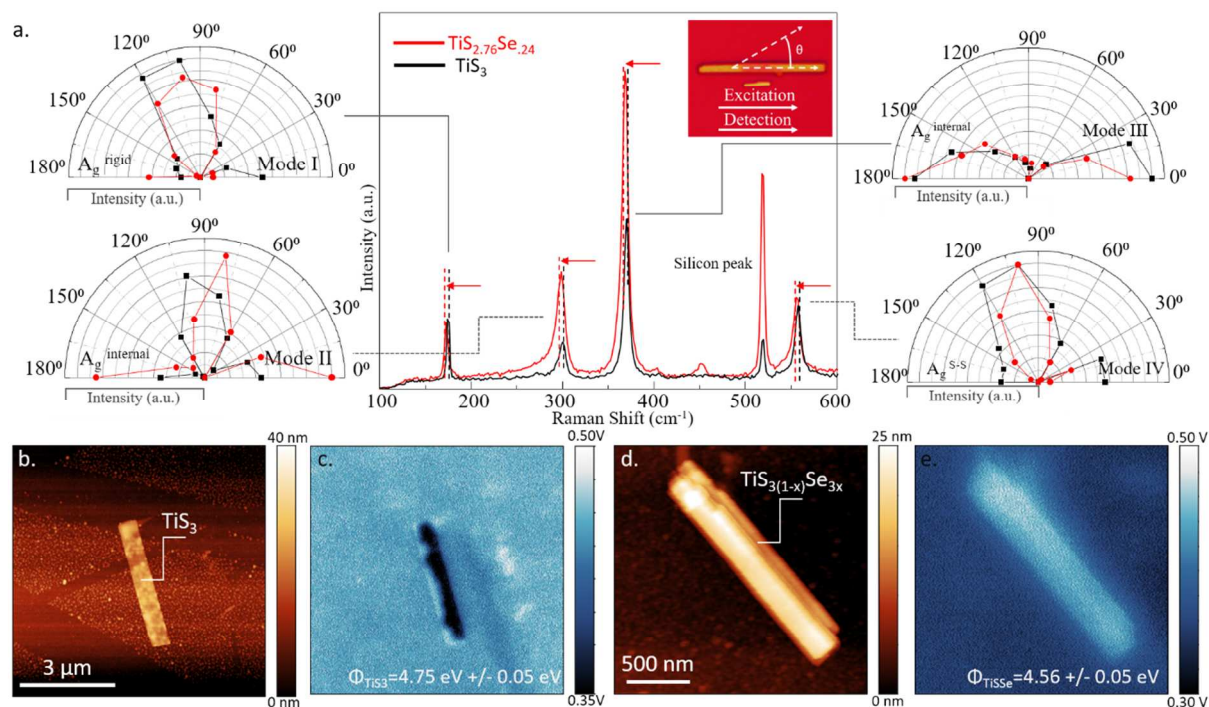


**Figure 3 a.** Raman spectrum of  $\text{TiS}_{2.76}\text{Se}_{.24}$  (red) and  $\text{TiS}_3$  (black) and polar plots for  $\text{TiS}_{2.76}\text{Se}_{.24}$  (red) and  $\text{TiS}_3$  (black) corresponding to all four modes in the spectrum. Here, silicon Raman peak intensity change might be related to relative orientation of polarization vector to the lattice direction (silicon intensity varies with respect to polarization direction) **b** and **d**. Shows AFM scans of  $\text{TiS}_3$  and  $\text{TiS}_{2.76}\text{Se}_{.24}$  sheets exfoliated on  $\text{SiO}_2/\text{Si}$  substrates, and **c**. and **e**. corresponds to surface potential scans (KPFM) on these two sheets.

**The degree of anisotropy in TMTCs alloys.** Another important crystallographic consideration in TMTCs involves the degree of anisotropy which describes how well pseudo-1D chains align with each other along the chain [100] lattice direction. This is of particular concern in TMTCs alloys since previous studies have demonstrated that the presence of point defects in 2D anisotropic material systems such as  $\text{ReS}_2$  and  $\text{ReSe}_2$  reduce the anisotropic response by randomizing pseudo-1D chains<sup>19-21</sup>. Angle-resolved Raman spectroscopy measurements were performed on a number of exfoliated  $\text{TiS}_{3(1-x)}\text{Se}_{3x}$  sheets to assess the degree of anisotropy. Previously, this method has been widely employed in the literature to determine the crystalline (chain) orientation and to determine the degree of anisotropy on 2D anisotropic material systems<sup>21-25</sup>.

Raman peaks located at  $176\text{ cm}^{-1}$  (mode I),  $296\text{ cm}^{-1}$  (mode II),  $368\text{ cm}^{-1}$  (mode III), and  $550\text{ cm}^{-1}$  (mode IV) are consistent with prior results on  $\text{TiS}_3$  and correspond to the out-of-phase rigid chain vibrations (mode I),  $A_g$ -like internal chain vibration (mode II and III), and chalcogen-chalcogen vibration (mode IV), respectively<sup>16,26,2</sup>. Out of these modes, mode III ( $\sim 368\text{ cm}^{-1}$ ) is of particular interest since it involves atomic vibrations along the chain [100] direction. The other Raman peaks exhibit more complex polar responses that are linked to Raman tensor properties. These I, II, and IV modes are not directly related to anisotropy and will be not discussed. Plotting Raman intensity of mode III with respect to the laser polarization direction, however, creates 2D polar plot which can be easily associated with the lattice (chain) direction of the nanoflakes, and Raman intensity ratio  $\eta = I_{\theta=0}/I_{\theta=90}$  that can be used as a gauge for the degree of anisotropy<sup>28</sup>. Here,  $I_{\theta=0}$  and  $I_{\theta=90}$  corresponds to mode III Raman intensity when laser polarization is parallel ( $\theta=0$ ) and perpendicular ( $\theta=90$ ) to the chain axis. As seen in Figure 3, both  $\text{TiS}_3$

and  $\text{TiS}_{3(1-x)}\text{Se}_{3x}$  exhibit similar  $\eta$  values ( $\sim 20$ ) and thus the degree of anisotropy as well as the anisotropic nature of the Ti-based TMTCs remain largely unchanged after Se alloying.

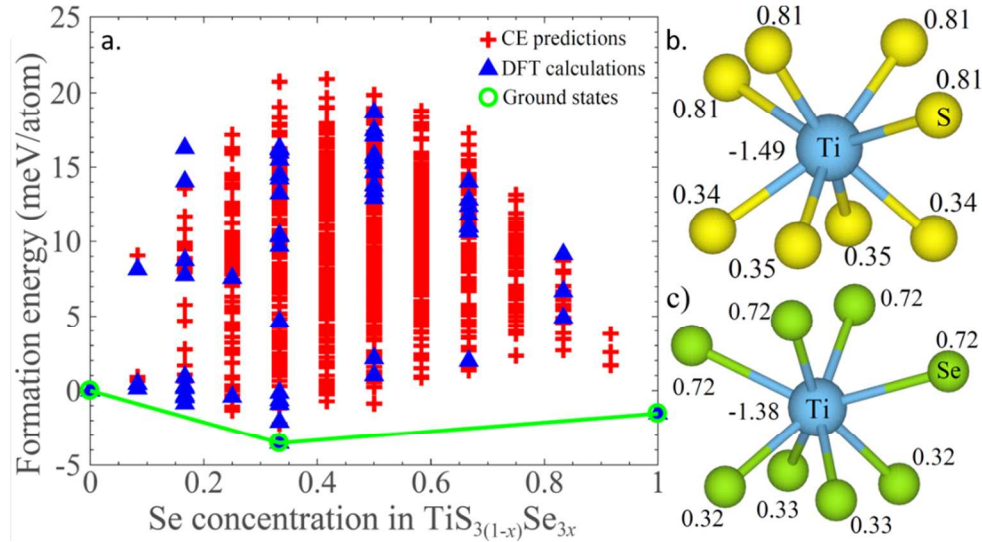


**Figure 4 a.** Calculated formation energies ( $E_f$ ) of  $\text{TiS}_{3(1-x)}\text{Se}_{3x}$  as a function of the selenium concentration ( $x$ ). Bader charge transfer analysis for **b.**  $\text{TiS}_3$  and **c.**  $\text{TiSe}_3$ , respectively.

Kelvin probe force microscopy (KPFM) measurements on exfoliated  $\text{TiS}_3$  and  $\text{TiS}_{3(1-x)}\text{Se}_{3x}$  sheets show that alloying selenium effectively reduces the electron affinity of the exfoliated sheets from 4.75 eV to 4.56 eV  $\Delta\Phi=0.19$  eV which corresponds to  $\sim 4\%$  reduction (Figure 3b-e). We note that the thickness values of  $\text{TiS}_3$  and  $\text{TiS}_{3(1-x)}\text{Se}_{3x}$  were kept nearly identical to each other ( $\sim 25$  nm see Figure 3b and d) to eliminate variation in the work functions due to thickness effects<sup>29</sup>. The thickness value was also kept much thicker than 10 nm to prevent localized charges at the  $\text{SiO}_2$  interface, which would influence the results. In principle, electronic doping in semiconductors does not largely influence the electron affinity values but has minor effect mostly associated with the increase in electron population at the conduction band. Since Se Bohr radius is larger than S and substantial amount of Se in  $\text{TiS}_3$  ( $x=0.08$ ), the energy required to take electron from conduction band to vacuum level (electron affinity) might be lowered by larger bonding distance and weaker covalent bonding strength. However, more studies are needed to shed detailed light into affinity changes in this ternary alloy system. Confidently, the affinity changes originate from selenium incorporation into  $\text{TiS}_3$  and offer a guideline for researchers to design solid-state devices (Schottky,  $p$ - $n$ , or ohmic contacts) with this alloying paradigm in mind.

**Cluster expansion theory and discussion.** Lastly, we discuss the fundamental origin of the narrow window for alloying in  $\text{TiS}_{3(1-x)}\text{Se}_{3x}$  ternary alloys. In our studies, we employed the cluster expansion method to search for stable compounds  $\text{TiS}_{3(1-x)}\text{Se}_{3x}$ . Figure 4a shows the formation energy  $E_f$  of  $\text{TiS}_{3(1-x)}\text{Se}_{3x}$  as a function of selenium concentration  $x$ . The  $E_f$  is calculated using the energies of  $\text{TiS}_3$  (set to zero) and  $\text{TiSe}_3$  with monoclinic structures. We observe there is only one stable alloy composition located at  $x = 1/3$ . Although this concentration deviates from the exact solution limit ( $x \cong 0.1$ ) found in the experiment, there exist a number of compounds with their (cluster expansion, CE) predicted or DFT  $E_f$  close to the boundary of the convex hull in the S-rich region, indicating that these compounds could be stable. However, to model a  $\text{TiS}_{3(1-x)}\text{Se}_{3x}$  structure with a small  $x$  requires a significantly large supercell, which is beyond the capability of DFT calculations. By contrast, few predicted  $\text{TiS}_{3(1-x)}\text{Se}_{3x}$  compounds have their  $E_f$  values near the convex hull, implying that Se-rich  $\text{TiS}_{3(1-x)}\text{Se}_{3x}$  compounds are unstable, which is consistent with the experiment. We also note that another source for deviation between theory

and experiment could potentially be related to our inability to properly account for interlayer coupling or complex orbital interactions in Ti based 2D material systems as recently pointed out by Kasai et al.<sup>30</sup>, in  $\text{TiS}_2$ .

To gain insight on the electronic mechanism of the solution limit of Se, we computed the Bader charge transfer of  $\text{TiS}_3$  and  $\text{TiSe}_3$ . Ti atoms in both compounds locate at an unusual chemical environment. Instead of common six-fold coordination as in  $\text{TiS}_2$ , each Ti atom has eight nearest-neighboring S or Se atoms. These S or Se atoms are also quite different in the same compound of  $\text{TiS}_3$  or  $\text{TiSe}_3$ , as we can see from the Bader charge transfer displayed in Figure 4b-c. For example, Fig.4b shows that the Bader charge transfer of the four S atoms above the Ti atom is much larger than that of the four S atoms below. In particular, a S atom above the Ti atom receives more electrons (0.81) in comparison with a S atom below (0.35). Replacing S atoms in  $\text{TiS}_3$  with Se atoms decreases the Bader charge transfer from 0.81 to 0.72 electrons due to the reduced electronegativity. Meanwhile, the Bader charge transfer is also reduced for the Ti atoms from 1.49 to 1.38 electrons. As a result of the combined electrostatic effects, the Coulomb interactions between chalcogen and Ti atoms is weakened leading to the instability of  $\text{TiSe}_3$ . A solution limit therefore occurs at a critical concentration of Se.

Overall, our results mark the first report on alloying in titanium based vdW pseudo-1D trichalcogenides which has been recently predicted to have a potential impact in optoelectronics and quantum optics owing to their high carrier mobility values, direct gap semiconductor nature, and direction dependent behavior. Observed alloying effects were found to be vastly different from those observed in 2D  $\text{TiS}_{2(1-x)}\text{Se}_{2x}$ ,  $\text{MX}_{2(1-x)}\text{Y}_{2x}$  (M=Mo, W, Re, Ti and X,Y=S, Se, and Te). Our TEM, EDS, Raman, XRD, and KPFM experimental results, together with theoretical cluster expansion analysis, provide deep insights into alloying behavior in these 2D anisotropic trichalcogenides material systems which is essential to understanding their true potential in the field.

## Methods

*Cluster expansion theory:* We used the Vienna *Ab initio* Simulation Package (VASP, version 5.4.4)<sup>31</sup> for density functional theory calculations. We obtained models of  $\text{TiS}_{3(1-x)}\text{Se}_{3x}$  structures with various Se concentrations  $x$  using the cluster expansion method as implemented in the ATAT package.<sup>32</sup> In all of the VASP calculations, we used the Perdew-Burke-Ernzerhof functional<sup>33</sup> and potential data sets generated from the projector augmented-wave method.<sup>34,35</sup> In addition, a kinetic energy cutoff of 500 eV was applied to set a limit to the number of plane waves. We also adopted an effective  $U$  parameter of 3.5 eV to treat the  $d$  orbitals of Ti atoms.<sup>36</sup>

*Material growth:* The  $\text{TiS}_{3(1-x)}\text{Se}_{3x}$  ternary alloy were synthesized using chemical vapor transport (CVT) method using elemental titanium (Sigma Aldrich, 99.99%), sulfur (Sigma Aldrich, 99.998%), and selenium (Alfa Aesar, 99.999%) as precursors. The precursors were mixed and loaded into pre-cleaned and heated quartz ampoules with the  $x$  values kept at 0.2, 0.4, 0.6 and 0.8, respectively. The ampule was then evacuated (to less than  $10^{-5}$  Torr), sealed, and placed in a two-zone furnace. The hot zone of the furnace was kept at  $550 \pm 1$  °C with temperature difference of  $4.5 \pm 0.1$  °C/cm over a distance of 21 cm. After 7 days, the ampule was naturally cooled to room temperature, and crystals were found at the interior wall of the ampoule.

*Material characterization:* The scanning electron microscopy (SEM) and energy-dispersive X-ray spectroscopy (EDS) mapping were performed using Hitachi S4700 field emission SEM. The working distance and the acceleration voltage was set as 12.9 mm and 15 kV, respectively. The transmission electron microscopy (TEM)

image and the diffraction pattern were measured by FEI Titan 80–300 TEM at 300 keV with a spherical aberration corrector. The thickness of exfoliated TiSSe samples was measured using Dimension Multimode 8 atomic force microscopy (AFM) under tapping mode. A typical scan rate was set to 1.0 Hz with a resolution of  $256 \times 256$ . The powder X-ray diffraction (XRD) measurement of the as-grown TiSSe whiskers was performed using Cu K $\alpha$  irradiation on PANalytical X'Pert PRO MRD X-Ray diffraction spectrometer. The Raman spectroscopy was performed under a backscattering geometry using a green laser ( $\lambda = 532$  nm) as the excitation source with an Andor 750 spectrometer. During the measurements, the incident light and the scattered light were aligned parallel to each other. In the angle-dependent Raman measurements, the angle  $\alpha$  was defined as the angle between *b*-axis and excitation laser; the  $\alpha$  angle was increased from  $0^\circ$  to  $180^\circ$  with a  $15^\circ$  step size by rotating a half-wave plate.

TEM Experimental section: Sample were prepared by first exfoliation onto SiO<sub>2</sub> substrate and then a 200 mesh holey carbon copper grid was put on top. A IPA droplet was used to cover the sample/holey carbon structure and air-dried and followed by etching SiO<sub>2</sub> away in 2mol/L KOH solution. Finally, holey carbon film with samples were cleaned by DI water. The transmission electron microscopy (TEM) image and the diffraction pattern were measured by FEI Titan 80–300 TEM at 300 keV with a spherical aberration corrector. SAED patterns were collected by a 10  $\mu$ m size aperture with a camera length of 380 mm.

## Acknowledgements

This work was partially funded by the National Science Foundation (EEC-1449500) Nanosystems Engineering Research Center on Nano-Enabled Water Treatment. S. T. acknowledges support from NSF DMR-1552220 and Army Research Office W911NF1710255. L. Liu and H. L. Zhuang thank the start-up funds from Arizona State University. This work also used computational resources of the Texas Advanced Computing Center under Contract No. TG-DMR170070.

## References

- 1 Kang, J., Tongay, S., Li, J. B. & Wu, J. Q. Monolayer semiconducting transition metal dichalcogenide alloys: Stability and band bowing. *J. Appl. Phys.* 113, doi:10.1063/1.4799126 (2013).
- 2 Lin, J. et al. Anisotropic Ordering in 1T' Molybdenum and Tungsten Ditelluride Layers Alloyed with Sulphur and Selenium. *ACS Nano*, doi:10.1021/acs.nano.7b08782 (2018).
- 3 Wang, G. et al. Spin-orbit engineering in transition metal dichalcogenide alloy monolayers. 6, 10110, doi:10.1038/ncomms10110 (2015).
- 4 Huang, B., Yoon, M., Sumpter, B. G., Wei, S.-H. & Liu, F. Alloy Engineering of Defect Properties in Semiconductors: Suppression of Deep Levels in Transition-Metal Dichalcogenides. *Phys. Rev. Lett.* 115, 126806 (2015).
- 5 Tongay, S. et al. Two-dimensional semiconductor alloys: Monolayer Mo<sub>1-x</sub>W<sub>x</sub>Se<sub>2</sub>. *Applied Physics Letters* 104, 4, doi:10.1063/1.4834358 (2014).
- 6 Wang, H., Yuan, H., Sae Hong, S., Li, Y. & Cui, Y. Physical and chemical tuning of two-dimensional transition metal dichalcogenides. *Chemical Society Reviews* 44, 2664-2680, doi:10.1039/C4CS00287C (2015).
- 7 Xie, L. M. Two-dimensional transition metal dichalcogenide alloys: preparation, characterization and applications. *Nanoscale* 7, 18392-18401, doi:10.1039/C5NR05712D (2015).
- 8 Joshua, O. I. et al. Electronics and optoelectronics of quasi-1D layered transition metal trichalcogenides. *2D Materials* 4, 022003 (2017).

- 9 Island, J. O. et al. Titanium trisulfide (TiS<sub>3</sub>): a 2D semiconductor with quasi-1D optical and electronic properties. *Scientific Reports* 6, 22214, doi:10.1038/srep22214 (2016).
- 10 Biele, R. et al. Strain-induced band gap engineering in layered TiS<sub>3</sub>. *Nano Res.* 11, 225-232, doi:10.1007/s12274-017-1622-3 (2018).
- 11 Aierken, Y., Cakr, D. & Peeters, F. M. Strain enhancement of acoustic phonon limited mobility in monolayer TiS<sub>3</sub>. *Physical Chemistry Chemical Physics* 18, 14434-14441, doi:10.1039/C6CP01809B (2016).
- 12 Lee, S. et al. Anisotropic in-plane thermal conductivity of black phosphorus nanoribbons at temperatures higher than 100 K. *Nature Communications* 6, 8573, doi:10.1038/ncomms9573 (2015).
- 13 Pant, A. et al. Strong Dichroic Emission in Pseudo One Dimensional Material ZrS<sub>3</sub>. *Nanoscale*, doi:10.1039/C6NR05238J (2016).
- 14 Wang, X. et al. Highly anisotropic and robust excitons in monolayer black phosphorus. *Nat Nano* 10, 517-521, doi:10.1038/nnano.2015.71 (2015).
- 15 Ferrer, I. J., et al. "Optical properties of titanium trisulphide (TiS<sub>3</sub>) thin films." *Thin Solid Films* 535 (2013): 398-401.
- 16 Wu, K. et al. Unusual lattice vibration characteristics in whiskers of the pseudo-one-dimensional titanium trisulfide TiS<sub>3</sub>. 7, 12952, doi:10.1038/ncomms12952 (2016).
- 17 Kang, J. & Wang, L.-W. Robust band gap of TiS<sub>3</sub> nanofilms. *Physical Chemistry Chemical Physics* 18, 14805-14809, doi:10.1039/C6CP01125J (2016).
- 18 Lipatov, A. et al. Few-layered titanium trisulfide (TiS<sub>3</sub>) field-effect transistors. *Nanoscale* 7, 12291-12296, doi:10.1039/C5NR01895A (2015).
- 19 Wu, K. et al. Domain Architectures and Grain Boundaries in Chemical Vapor Deposited Highly Anisotropic ReS<sub>2</sub> Monolayer Films. *Nano Letters* 16, 5888-5894, doi:10.1021/acs.nanolett.6b02766 (2016).
- 20 Lin, Y.-C. et al. Single-Layer ReS<sub>2</sub>: Two-Dimensional Semiconductor with Tunable In-Plane Anisotropy. *ACS Nano* 9, 11249-11257, doi:10.1021/acsnano.5b04851 (2015).
- 21 Chenet, D. A. et al. In-Plane Anisotropy in Mono- and Few-Layer ReS<sub>2</sub> Probed by Raman Spectroscopy and Scanning Transmission Electron Microscopy. *Nano Letters* 15, 5667-5672, doi:10.1021/acs.nanolett.5b00910 (2015).
- 22 Kong, W. et al. Angle resolved vibrational properties of anisotropic transition metal trichalcogenide nanosheets. *Nanoscale* 9, 4175-4182, doi:10.1039/C7NR00711F (2017).
- 23 Huang, S. et al. In-Plane Optical Anisotropy of Layered Gallium Telluride. *ACS Nano*, doi:10.1021/acsnano.6b05002 (2016).
- 24 Chen, B. et al. Controlling Structural Anisotropy of Anisotropic 2D Layers in Pseudo-1D/2D Material Heterojunctions. *Advanced Materials* 29, 1701201, doi:10.1002/adma.201701201 (2017).
- 25 Philipp, N., Gerd, P., Christian, S. & Tobias, K. Observation of anisotropic interlayer Raman modes in few-layer ReS<sub>2</sub>. *physica status solidi (RRL) – Rapid Research Letters* 10, 185-189, doi:10.1002/pssr.201510412 (2016).
- 26 Kang, J., Sahin, H., Ozaydin, H. D., Senger, R. T. & Peeters, F. M. TiS<sub>3</sub> nanoribbons: Width-independent band gap and strain-tunable electronic properties. *Physical Review B* 92, 075413 (2015).
- 27 Island, J. O. et al. TiS<sub>3</sub> Transistors with Tailored Morphology and Electrical Properties. *Advanced Materials* 27, 2595-2601, doi:10.1002/adma.201405632 (2015).
- 28 Yang, S. et al. Environmental stability of 2D anisotropic tellurium containing nanomaterials: anisotropic to isotropic transition. *Nanoscale* 9, 12288-12294, doi:10.1039/C7NR02397A (2017).
- 29 Silva-Guillén, J. A., Canadell, E., Ordejón, P., Guinea, F. & Roldán, R. Anisotropic features in the electronic structure of the two-dimensional transition metal trichalcogenide TiS<sub>3</sub>: electron doping and plasmons. *2D Materials* 4, 025085 (2017).
- 30 Kasai, H. et al. X-ray electron density investigation of chemical bonding in van der Waals materials. *Nature Materials* 17, 249-252, doi:10.1038/s41563-017-0012-2 (2018).
- 31 Kresse, G. & Furthmüller, J. Efficient iterative schemes for ab initio total-energy calculations using a plane-wave basis set. *Phys. Rev. B* 54, 11169-11186 (1996).
- 32 Van de Walle, A. Multicomponent multisublattice alloys, nonconfigurational entropy and other additions to the Alloy Theoretic Automated Toolkit. *Calphad* 33, 266-278 doi:<https://doi.org/10.1016/j.calphad.2008.12.005> (2009).
- 33 Perdew, J. P., Burke, K. & Ernzerhof, M. Generalized Gradient Approximation Made Simple. *Phys. Rev. Lett.* 77, 3865-3868 (1996).

- 34 Blöchl, P. E. Projector augmented-wave method. *Phys. Rev. B* 50, 17953-17979 (1994).
- 35 Kresse, G. & Joubert, D. From ultrasoft pseudopotentials to the projector augmented-wave method. *Phys. Rev. B* 59, 1758-1775 (1999).
- 36 Dudarev, S. L., Botton, G. A., Savrasov, S. Y., Humphreys, C. J. & Sutton, A. P. Electron-energy-loss spectra and the structural stability of nickel oxide: An LSDA+U study. *Phys. Rev. B* 57, 1505-1509, doi:10.1103/PhysRevB.57.1505 (1998)

